

AUTOMATED ANALYSIS OF SCATTERING-BASED LIGHT  
SHEET MICROSCOPY IMAGES OF ANAL SQUAMOUS  
INTRAEPITHELIAL LESIONS

by

Yong Jun Kim

---

Copyright © Yong Jun Kim 2024

A Thesis Submitted to the Faculty of the

DEPARTMENT OF BIOMEDICAL ENGINEERING

In Partial Fulfillment of the Requirements

For the Degree of

MASTER OF SCIENCE

In the Graduate College

THE UNIVERSITY OF ARIZONA

2024

THE UNIVERSITY OF ARIZONA  
GRADUATE COLLEGE

As members of the Master's Committee, we certify that we have read the thesis prepared by Yong Jun Kim, titled *Automated Analysis of Scattering-Based Light Sheet Microscopy Images of Anal Squamous Intraepithelial Lesions* and recommend that it be accepted as fulfilling the dissertation requirement for the Master's Degree.

*Dongkyun Kang*

\_\_\_\_\_  
*Dongkyun Kang, PhD*

Date: 12/12/2024

*Travis Sawyer*

\_\_\_\_\_  
*Travis Sawyer, PhD*

Date: 12/12/2024

*Vignesh Subbian*

\_\_\_\_\_  
Vignesh Subbian (Dec 12, 2024 13:33 MST)

*Vignesh Subbian, PhD*

Date: 12/12/2024

Final approval and acceptance of this thesis is contingent upon the candidate's submission of the final copies of the thesis to the Graduate College.

I hereby certify that I have read this thesis prepared under my direction and recommend that it be accepted as fulfilling the Master's requirement.

*Dongkyun Kang*

\_\_\_\_\_  
*Dongkyun Kang, PhD*  
Master's Thesis Committee Chair  
*Biomedical Engineering*

Date: 12/12/2024

ARIZONA

## ACKNOWLEDGMENTS

I would like to express my sincere gratitude to my advisor, Dr. Dongkyun Kang, for his invaluable guidance and support throughout my academic journey. His mentorship and insights have been fundamental to my growth, and I am thankful for the opportunities he provided to learn and develop new skills.

I would also like to my sincere thanks to my thesis committee members, Dr. Travis William Sawyer and Dr. Vignesh Subbian. I deeply appreciate their time and willingness to provide guidance and feedback during this key step in my academic journey.

I am grateful to my collaborators, Dr. Eric Yang, Dr. Michelle Joanne Khan, and Dr. Brooke Liang at Stanford University for their invaluable contributions to the research discussed in this thesis. I would also like to thank my collaborators Dr. Koeun Lim and Dr. Denise Roe for their guidance and assistance, which were instrumental in completing this work.

A special thanks to my lab mates in the Translational Optical Imaging Lab, including my mentor Jingwei Zhao, Momoka Sugimura, Kennth Marcelino, Rafael Romero, Paige Sawyers, Ameer Nessae, Carmella Ocaya, Michael Gnesda, Kayma Konecny, Jason Datta, Adiba Haque, Tara Petel, and Kian Ali Sadat. Their support and collaboration have made the challenges of research more rewarding and enjoyable.

## TABLE OF CONTENTS

<b>LIST OF FIGURES .....</b>	<b>5</b>
<b>LIST OF TABLES .....</b>	<b>6</b>
<b>ABSTRACT .....</b>	<b>7</b>
<b>CHAPTER 1: INTRODUCTION.....</b>	<b>8</b>
<b>CHAPTER 2: AUTOMATED ANALYSIS OF SCATTERING-BASED LIGHT SHEET MICROSCOPY IMAGES OF ANAL SQUAMOUS INTRAEPITHELIAL LESIONS .....</b>	<b>9</b>
<b>2.1 INTRODUCTION.....</b>	<b>9</b>
<b>2.2 MATERIALS AND METHODS .....</b>	<b>12</b>
<i>2.2.1 Scattering-Based Light Sheet Microscopy .....</i>	<i>12</i>
<i>2.2.2 Image Pre-processing .....</i>	<i>13</i>
<i>2.2.3 Automated Segmentation of Nuclei.....</i>	<i>14</i>
<i>2.2.4 Feature Calculations .....</i>	<i>17</i>
<i>2.2.5 Classifier Development and Evaluation.....</i>	<i>18</i>
<b>2.3 RESULTS .....</b>	<b>20</b>
<i>2.3.1 Feature Analysis.....</i>	<i>20</i>
<i>2.3.2 Classifier Performance .....</i>	<i>23</i>
<b>2.4 DISCUSSION AND CONCLUSION.....</b>	<b>25</b>
<b>FUNDING.....</b>	<b>27</b>
<b>ACKNOWLEDGMENTS.....</b>	<b>27</b>
<b>DISCLOSURES .....</b>	<b>27</b>
<b>DATA AVAILABILITY .....</b>	<b>28</b>
<b>CHAPTER 3: CONCLUSIONS .....</b>	<b>29</b>
<b>REFERENCES .....</b>	<b>30</b>

## LIST OF FIGURES

<b>Figure 2.1:</b> Schematic diagram of sLSM .....	13
<b>Figure 2.2:</b> Representative sLSM images of non-dysplastic (a), LSIL (b), and HSIL (c).....	13
<b>Figure 2.3:</b> Image pre-processing workflow .....	14
<b>Figure 2.4:</b> Row-by-row binarization of sLSM image. (a) sLSM image with the yellow line indicating the row for intensity profile, (b) intensity profile before background subtraction, (c) intensity profile after background subtraction, and (d) binarized intensity profile .....	15
<b>Figure 2.5:</b> Automated nuclear segmentation and analysis of nuclear morphometric features for representative LSIL and HSIL images. (a, b) sLSM images, (c, d) manually-segmented images, (e, f) automatically-segmented images using the row-by-row binarization, (g, h) automatically-segmented images using StarDist, (i, j) nuclear-to-nuclear distance estimation using Delaunay neighbors, and (k, l) nuclear-to-cytoplasmic ratio estimation using Voronoi diagrams.....	17
<b>Figure 2.6:</b> Two-dimensional scatter plots of feature distributions for three diagnostic categories: non-dysplastic (green), LSIL (yellow), and HSIL (red). (a) Nuclear intensity versus intensity slope, (b) nuclear-to-nuclear distance versus N/C ratio, (c) cell density versus nuclear area, and (d) cell density versus proportion of nuclear pixels .....	21
<b>Figure 2.7:</b> Scatter plots of features and their average values with 95% confidence intervals. (a) nuclear intensity, (b) intensity slope, (c) nuclear-to-nuclear distance, (d) N/C ratio, (e) cell density, (f) nuclear area, and (g) proportion of nuclear pixels. ND – non-dysplastic .....	22
<b>Figure 2.8:</b> ROC curves for diagnostic performance evaluation. (a) ROC curve for per-image diagnosis, and (b) ROC curve for per-biopsy diagnosis. red circles – operating points for automated classification, green square – operating point for manual diagnosis of H&E images, and blue square – operating point for manual diagnosis of sLSM images .....	24
<b>Figure 2.9:</b> Classification scores for non-HSIL and HSIL images. black circles – scores for images of biopsies that went through p16, and white circles – scores for images without p16 .....	25

## LIST OF TABLES

<b>Table 2.1:</b> One-way ANOVAs and multiple comparisons between non-dysplastic (ND), LSIL, and HSIL.....	23
<b>Table 2.2:</b> Sensitivity, specificity, and accuracy (95% confidence interval) of automated classification of sLSM images in comparison to those of manual diagnosis of sLSM and H&E images .....	24

## ABSTRACT

Anal cancer presents diagnostic challenges, particularly in identifying high-grade squamous intraepithelial lesions (HSIL), with its increasing incidence and mortality rates. Current diagnosis methods, including cytology, biopsy, and high resolution anoscopy (HRA), provide important diagnostic information. However, cytology is often limited by suboptimal sensitivity and specificity, while high resolution anoscopy-guided biopsy is limited by its long processing times due to unnecessary biopsies and staining requirements. Scattering-based light sheet microscopy (sLSM) can offer an alternative approach by utilizing intrinsic tissue scattering properties to visualize morphologic features without the need for additional labeling or staining.

In this study, we developed and evaluated an automated algorithm for analyzing 187 sLSM images obtained from 80 anal biopsies. The method employed a row-by-row binarization technique for nuclear segmentation, achieving high precision (0.97) and recall (0.91). Seven nuclear features, including nuclear intensity, intensity slope as a function of depth, nuclear-to-nuclear distance, nuclear-to-cytoplasm ratio, cell density, nuclear area, and proportion of pixels corresponding to nuclei were extracted and statistically analyzed. Among the seven features, six showed statistically significant differences between HSIL and non-HSIL (non-dysplastic or low-grade squamous intraepithelial lesion, LSIL).

A linear support vector machine (SVM) was trained and tested using five-fold cross validation on these features. The classifier achieved a sensitivity of 90%, specificity of 70%, and area under the curve (AUC) of 0.89 for per-image diagnosis, and sensitivity of 90%, specificity of 80%, and area under the curve (AUC) of 0.93 for per-biopsy diagnosis.

## CHAPTER 1

### INTRODUCTION

Light sheet microscopy (LSM) is an advanced imaging technology that has revolutionized the way researchers study biological specimens. The origins of this method was published in 1903 when Richard Zsigmondy and Henry Sidentopf introduced the ultramicroscope for observing colloidal particles by utilizing a planar illumination approach to achieve enhanced contrast [1]. Despite its early development, the LSM technique gained prominence in the early 2000s with the introduction of selective plane illumination microscopy (SPIM). SPIM enabled live imaging of entire organisms with minimal photodamage and phototoxicity and critically contributed the advancement for the biology studies [2].

The development of LSM has opened new ways for specialized applications in pathology and oncology. sLSM represents an adaptation of this technology, designed to utilize the scattering properties of tissue to generate intrinsic contrast. Unlike fluorescence-based methods that require labeling, sLSM uses scattered light to visualize tissue structures and nuclear morphology. This feature makes it a valuable tool for histopathological diagnostics, where it can highlight nuclei as bright intensity signals without the need for labeling.

In this thesis, we will explore the potential of sLSM in diagnosing anal squamous intraepithelial lesions using rule-based image analysis. Chapter 2 details the analysis of sLSM images through the extraction of nuclear features, including size, shape, and density, which are key indicators of dysplasia. These features are incorporated into an automated analysis pipeline to assess the diagnostic performance of sLSM in distinguishing HSIL from non-HSIL.

## CHAPTER 2

### AUTOMATED ANALYSIS OF SCATTERING-BASED LIGHT SHEET MICROSCOPY IMAGES OF ANAL SQUAMOUS INTRAEPITHELIAL LESIONS

This chapter was published as: Yongjun, Kim, et al. “Automated analysis of scattering-based light sheet microscopy images of anal squamous intraepithelial lesions.” *Biomedical optics express* 15.9 (2024): 5547-5559. [URL:https://opg.optica.org/boe/fulltext.cfm?uri=boe-15-9-5547&id=557185](https://opg.optica.org/boe/fulltext.cfm?uri=boe-15-9-5547&id=557185)  
©2024 Optica Publishing Group under the terms of the Optica Open Access Publishing Agreement

#### 2.1 INTRODUCTION

Anal cancer is an under-served disease with rapidly increasing incidence and mortality. The incidence of anal squamous carcinoma increased by 2.7% per year between 2001 and 2015. Within this period, both incidence of higher stage disease and anal cancer mortality increased [3]. The trend continued, with the anal cancer mortality increasing by 5.7% per year between 2014 and 2020 [4]. The recent ANCHOR (Anal Cancer HSIL Outcomes Research) trial showed that treatment of anal precancer can significantly reduce the risk of anal cancer [5]. However, the standard methods for screening of anal cancer have limitations. Anal cytology via Pap smear is the first-line screening method, however, it provides moderate diagnostic performance, 81% sensitivity and 63% specificity for detecting anal precancer (high-grade squamous intraepithelial lesion, HSIL) [6]. Therefore, patients with abnormal anal cytology results need to undergo high-resolution anoscopy-guided biopsy to make the final diagnosis. High-resolution anoscopy provides magnified views of the anal tissue, however, it cannot visualize microscopic details of the tissue that are critical in accurately diagnosing anal lesions.

*In vivo* optical diagnostic methods can non-invasively examine microscopic details of the tissue. Previously, light scattering spectroscopy methods were evaluated for diagnosing HSIL of cervix tissues [7], which are biologically and histomorphologically similar to anal tissues [8]. In light scattering spectroscopy, differences in nuclear morphologic features (e.g. nuclear diameter) between HSIL and non-HSIL (non-dysplastic or low-grade intraepithelial lesion, LSIL) generate differences in light scattering spectra. A previous study evaluating light scattering spectroscopy demonstrated 77% sensitivity and 62% specificity for diagnosing cervical HSIL versus non-HSIL [7]. Angle-resolved low coherence interferometry (a/LCI) advanced light scattering spectroscopy further to investigate depth-resolved nuclear morphologic features. Recent *in vivo* imaging studies showed that a/LCI could provide great diagnostic performance, 100% sensitivity and 71-82% specificity for diagnosing HSIL versus non-HSIL in cervix [9]. Confocal microscopy is another promising *in vivo* optical diagnostic approach because it can directly visualize nuclei. In previous studies, quantitative analysis of confocal microscopy images of cervix provided a high sensitivity (100%) and specificity (92-100%) for diagnosing HSIL versus non-HSIL [10, 11]. High-resolution micro-endoscopy (HRME) is a low-cost *in vivo* microscopy approach that can also directly visualize nuclei. HRME showed a promising sensitivity of 84-97% and specificity of 54-74% for diagnosing high-grade cervical lesions in low-resource settings [12, 13]. More recently, HRME was evaluated for examining anal lesions *in vivo*. A deep learning-based model was used to analyze HRME images, which demonstrated great diagnostic performance, sensitivity of 91% and specificity of 87% [14, 15].

Scattering-based light sheet microscopy (sLSM) is another *in vivo* optical diagnostic approach that can visualize nuclei with a high resolution (lateral = 1-2  $\mu\text{m}$ ; axial = 5-6  $\mu\text{m}$ ) using intrinsic scattering contrast [16, 17]. In sLSM, the tissue is illuminated with light sheet

at 45° relative to the tissue surface, and scattered light is detected at 90° from the illumination beam with low-NA microscope optics. In a recent study, a bench sLSM device was evaluated for imaging anal biopsies *ex vivo* [18]. This study showed that sLSM could visualize key nuclear morphologic features used during standard of care histopathologic diagnosis of anal squamous intraepithelial lesions. Additionally, 11 pathologists made diagnosis based on sLSM images, which provided 91% sensitivity and 85% specificity for diagnosing HSIL versus non-HSIL [18]. The feasibility of integrating sLSM into a compact probe was also demonstrated recently [19].

One potential use case of sLSM is to guide anal biopsy. In this approach, the anoscopist first examines the anal mucosa with high-resolution anoscopy to identify areas suspicious of HSIL and images the suspicious areas with the sLSM probe. sLSM images are then analyzed to determine the probability of HSIL. This information can be used to ensure biopsy of likely HSIL tissues and avoid biopsy of obviously non-HSIL (non-dysplastic or LSIL) tissues. One critical task in this sLSM-guided biopsy approach is to interpret sLSM images at the time of anoscopy. Our previous study showed that pathologists were able to make accurate diagnosis based on sLSM images after a short training session of reviewing only 8 pairs of sLSM and hematoxylin and eosin (H&E) images. Therefore, training pathologists to read sLSM images might not be a significant hurdle. Once trained, the pathologist can analyze sLSM images in real time either at the anoscopy clinic or remotely.

However, relying on pathologist's interpretation could hamper the adoption of sLSM due to their limited availability. Automated analysis of sLSM images can mitigate this issue by providing real-time diagnostic information that the anoscopist can act upon. In this paper, we present the development of an algorithm for automatically analyzing sLSM images of anal squamous intraepithelial lesions. The processes for automatically segmenting sLSM images

for nuclei and generating image features are presented. Results from feature analysis and classifier development are also presented.

## **2.2 MATERIALS AND METHODS**

### *2.2.1 Scattering-Based Light Sheet Microscopy*

The working principle of sLSM was described previously [17]. Briefly, light from an LED (center wavelength = 640 nm; bandwidth = 25 nm) and a slit (width = 5  $\mu\text{m}$ ; length = 3mm) was focused as light sheet on the tissue by relay optics with the demagnification of 2 (Fig. 2.1). As the light sheet intersects the tissue, nuclei scatter a portion of the illumination light. The scattered light is captured by the detection objective lens (focal length = 20 mm; water immersion; NA = 0.3) and focused to generate a magnified image of the tissue. The bench sLSM device used for imaging anal biopsies *ex vivo* had the lateral resolution of 1.4  $\mu\text{m}$ , and axial resolution of 5.2  $\mu\text{m}$ . The anal biopsies were treated with a low-concentration acetic acid before sLSM imaging to enhance the nuclear contrast. The biopsy sample was translated laterally by a motorized stage with the step size of 100  $\mu\text{m}$ . An sLSM image was acquired at each lateral location. This made the vertical distance between two neighboring sLSM images along the tissue depth direction also 100  $\mu\text{m}$ . Neighboring sLSM images did not have any overlaps.

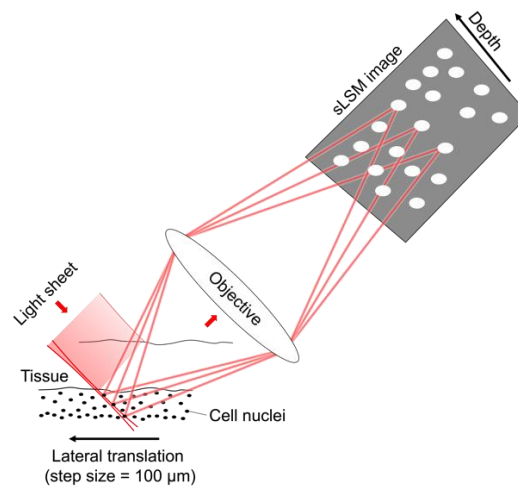


**Figure 2.1:** Schematic diagram of sLSM.

We used sLSM images of anal biopsies collected from our previous *ex vivo* study [18]. 187 sLSM images obtained from 80 biopsies were used in image analysis. Remaining 30 biopsies out of 110 biopsies from our previous study were not included in the automated image analysis because these 30 biopsies showed columnar epithelium, denuded tissue, or unclear nuclear contrast. Among the 80 biopsies, 14 were non-dysplastic, 36 were LSIL, and 30 were HSIL per final pathology report. Representative sLSM images are shown in Fig. 2.2. Nuclei are visualized as bright dots in these images.

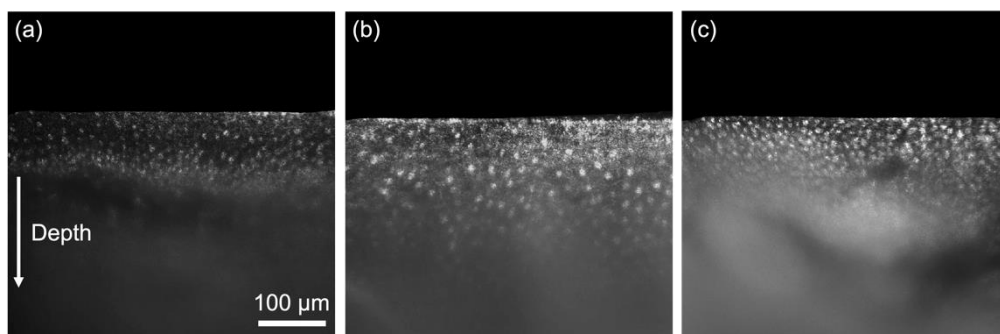


**Figure 2.2:** Representative sLSM images of non-dysplastic (a), LSIL (b), and HSIL (c).

### 2.2.2 Image Pre-processing

We used MATLAB 2024a (Mathworks) installed on a PC with the following specifications: Intel Core i9-12900F CPU, 32GB DDR5 RAM, NVIDIA GeForce RTX 3080

GPU with 10GB VRAM. sLSM images were pre-processed before nuclear segmentation and feature extraction. Each image was cropped to a size of  $1064 \times 1064$  pixels, which corresponds to  $500 \mu\text{m} \times 500 \mu\text{m}$  on the tissue space (Fig. 2.3a). Bright signal at the top generated by specular reflection of the tissue surface and/or imaging window was masked out using Gaussian filtering followed by binary thresholding (Fig. 2.3b). Next, the tissue surface was identified using adaptive binarization based on Otsu's method [20] and edge detection (Fig. 2.3c). The detected tissue surface was used as the reference to perform column shifting, flattening the tissue surface (Fig. 2.3d). The column-shifted image underwent another round of surface detection to identify the row index of the tissue surface (Fig. 2.3e). Most sLSM images were acquired with an exposure time of 0.1 seconds, but different exposure times were used for a small number of biopsies to adjust the brightness displayed during the image acquisition. The actual exposure time was used to standardize the image intensity to the reference exposure time of 0.1 seconds (Fig. 2.3f).

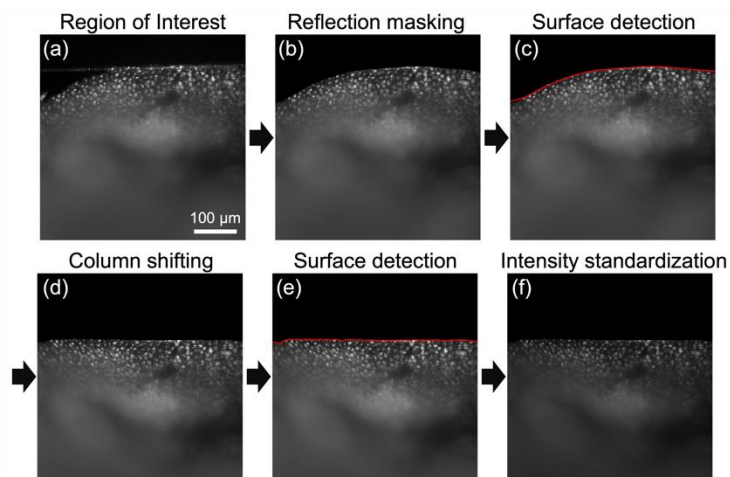


**Figure 2.3:** Image pre-processing workflow.

### 2.2.3 Automated Segmentation of Nuclei

Our overall approach is to segment sLSM images for nuclei and analyze morphometric features of the segmented nuclei. Each sLSM image visualizes nuclei at multiple depth levels,

and the nuclear contrast and intensity change as a function of depth within the image. Therefore, we developed a segmentation method that binarizes each row (or each depth) of the image at a time. At each row (yellow line in Fig. 2.4a), an intensity profile was generated (Fig. 2.4b). The background signal of the intensity profile was calculated by using a one-dimensional adaptation of the rolling ball background subtraction method [21] with the ball radius of 25 pixels. The background signal curve was then subtracted from the intensity profile (Fig. 2.4c). The binarization threshold (red dotted line in Fig. 2.4c) was calculated as the average of the 91<sup>st</sup> percentile intensity and 15<sup>th</sup> percentile intensity. The reference percentiles for threshold calculation were optimized via grid search to have a high precision and recall for segmenting nuclei as discussed later. Finally, the intensity profile was binarized by the threshold as shown in Fig. 2.4d. This process was repeated for every row to generate a two-dimensional binary mask showing nuclei.

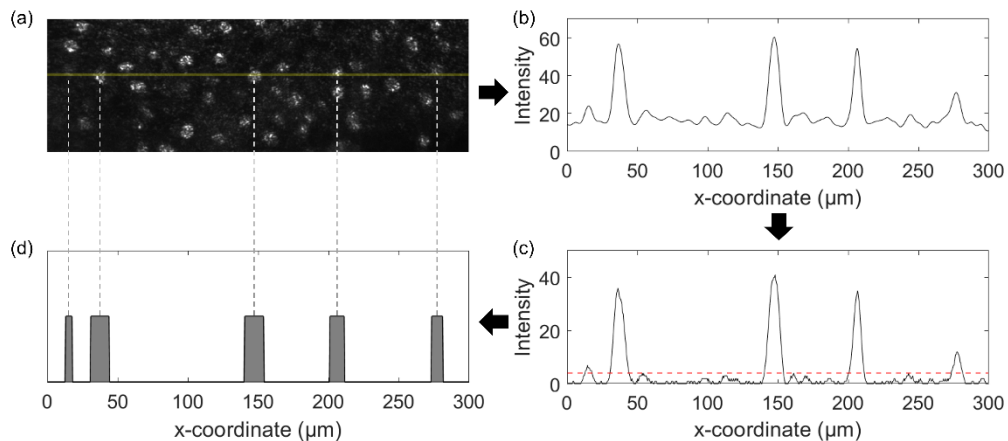


**Figure 2.4:** Row-by-row binarization of sLSM image. (a) sLSM image with the yellow line indicating the row for intensity profile, (b) intensity profile before background subtraction, (c) intensity profile after background subtraction, and (d) binarized intensity profile.

The segmentation performance was evaluated by comparing automatically-segmented nuclei to manually-segmented nuclei. 850 manually-segmented nuclei from 9 sLSM images (3 non-dysplastic, 3 LSIL, and 3 HSIL images) were used for evaluation (Figs. 2.5c, d). The row-by-row binarization method (Figs. 2.5e, f) provided good segmentation performance, precision

of 0.97 (95% confidence interval, CI = 0.95-0.98) and recall of 0.91 (95% CI = 0.88-0.92). The corresponding F1 score was 0.94.

We compared our row-by-row binarization approach to a deep learning-based cell segmentation method, StarDist [22]. The sLSM image (Figs. 2.5a,b) was background-subtracted using the two-dimensional rolling ball method [21] with a radius of 25 pixels. The background-subtracted image was segmented by the Fiji plugin implementation of StarDist. Various probability thresholds were evaluated for segmentation performance via grid search. When the threshold was set to produce the highest F1 score, 0.90, the precision was 0.90 (95% CI = 0.88-0.92) and recall was 0.91 (95% CI = 0.88-0.92). Figs. 2.5g,h show StarDist-segmented images at this probability threshold. It is notable that the StarDist-segmented HSIL image (Fig. 2.5h) shows some of the nuclei at deeper regions are not segmented, and segmented nuclei are smaller than the manually-segmented nuclei. The precision was 0.94 and recall was 0.86 for this StarDist-segmented image, while the precision was 0.97 and recall was 0.90 using the row-by-row binarization method (Fig. 2.5f). While the performance of StarDist might be further improved by fine-tuning, we decided to use the row-by-row binarization approach because of its better performance especially for HSIL images.

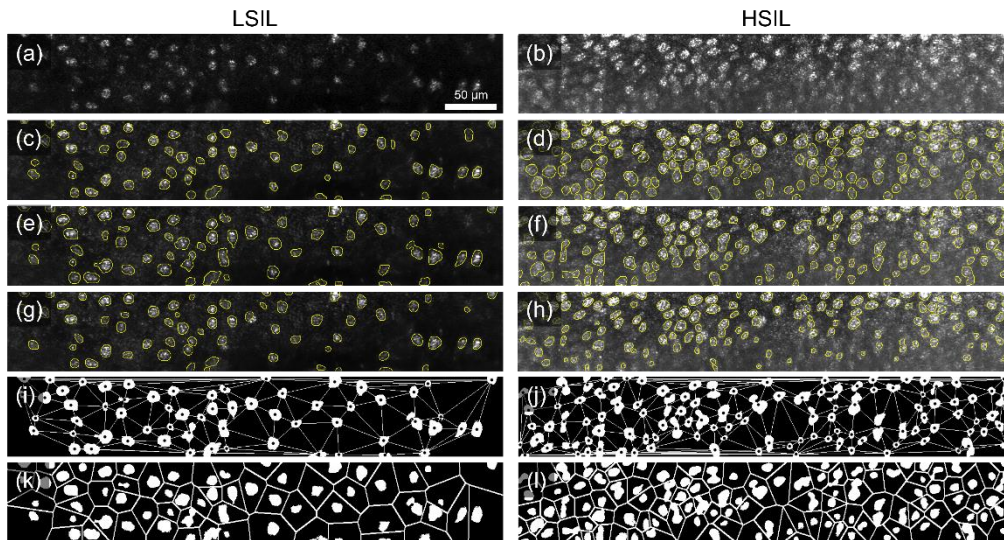


**Figure 2.5:** Automated nuclear segmentation and analysis of nuclear morphometric features for representative LSIL and HSIL images. (a, b) sLSM images, (c, d) manually-segmented images, (e, f) automatically-segmented images using the row-by-row binarization, (g, h) automatically-segmented images using StarDist, (i, j) nuclear-to-nuclear distance estimation using Delaunay neighbors, and (k, l) nuclear-to-cytoplasmic ratio estimation using Voronoi diagrams.

#### 2.2.4 Feature Calculations

Seven features were calculated from the automatically-segmented nuclei within the depth range of 20-100  $\mu\text{m}$ . The lower bound of 20  $\mu\text{m}$  was used to exclude any residual contribution of the surface specular reflection. The upper bound of 100  $\mu\text{m}$  was used because nuclear features were reliably visible up to the depth of 100  $\mu\text{m}$  in most sLSM images and also because previous confocal microscopy studies showed that the imaging depth of 50  $\mu\text{m}$  revealed nuclear morphologic features relevant for diagnosis of HSIL versus non-HSIL [10, 11].

The first two features were related to nuclear intensity. The sLSM image before background subtraction (Figs. 2.5a,b) was multiplied with the binary nuclear mask (Figs. 2.5e,f). Intensity values of non-zero pixels, also the pixels corresponding to nuclei, were averaged to calculate the representative nuclear intensity for each image. Nuclear intensity versus depth curve was generated using every row, and the slope of this curve was calculated by linear fitting. The linear fitting performance was acceptable with the average  $R^2$  value of 0.59 for all 187 images.

The next two features, nuclear-to-nuclear distance and nuclear-to-cytoplasmic ratio (N/C ratio), were estimated based on the approach previously developed for analyzing confocal microscopy images of cervical biopsies [11]. Nuclear-to-nuclear distance was calculated as the average of distances between a nucleus to its three closest Delaunay neighbors (Figs. 2.5i,j). N/C ratio was estimated by finding centroids of nuclei, generating a Voronoi diagram using the centroids (Figs. 2.5k,l), calculating the area of each Voronoi polygon (estimated cellular area) and the area of its enclosed nucleus (estimated nuclear area), and dividing the nuclear area by the difference between the cellular area and nuclear area (estimated cytoplasmic area).

The last three features were cell density, nuclear area, and proportion of nuclear pixels. Cell density was calculated by dividing the number of nuclei by the image area in the unit of  $\mu\text{m}^2$ . Nuclear area was calculated by averaging areas of nuclei. Proportion of nuclear pixels was calculated by dividing the number of non-zero pixels in the binary nuclear mask (Figs. 2.5e,f) by the number of all pixels of the image.

Statistical significance was assessed using one-way analysis of variance (ANOVA) and Bonferroni post-hoc multiple comparisons. The statistical analysis was conducted using the MATLAB 2024a Statistics and Machine Learning Toolbox.

### *2.2.5 Classifier Development and Evaluation*

We evaluated a linear support vector machine (SVM) classifier for diagnosing HSIL versus non-HSIL (non-dysplastic or LSIL). Classifications were made into two categories (non-HSIL, HSIL) instead of three (non-dysplastic, LSIL, HSIL). This is because HSIL finding would indicate immediate biopsy or treatment, while non-HSIL finding would indicate monitoring over time.

All seven features were used during the classifier development. Before training and testing, each feature was normalized by applying median interquartile range normalization. The dataset was then divided into training and testing sets. We evaluated classifier performance through a five-fold cross validation. The data was randomly divided into five folds. The data stratification was based on biopsies rather than images. This ensured that all feature data from each biopsy belonged to the same fold, making data from each biopsy used for either training or testing but not for both. Each fold included feature data from approximately 37 images obtained from 3 non-dysplastic, 7 LSIL, and 6 HSIL biopsies. Four folds (approximately 150 images from 12 non-dysplastic, 28 LSIL, and 24 HSIL) were used to train the classifier, and the remaining fold was used for testing. This process was repeated five times to test each image exactly once.

Classification scores for all 187 images were aggregated from the five folds. Classification scores and their corresponding histopathologic diagnoses were used to generate a receiver operating characteristic (ROC) curve for diagnosing HSIL versus non-HSIL. This ROC curve showed the performance of per-image diagnosis. We also evaluate the performance of per-biopsy diagnosis. For each biopsy, the minimum of classification scores was chosen as the representative score for the biopsy. We hypothesized that choosing the minimum score would reduce false positives and increase the specificity of diagnosing HSIL. The ROC curve for per-biopsy diagnosis was generated by comparing 80 classification scores from 80 biopsies with the corresponding histopathologic diagnoses. The area under the curve (AUC) was calculated for each ROC curve. In order to compensate for the imbalance in data (more non-HSIL data than HSIL data), the weight of false negatives in the cost function was optimized to maximize the AUC of the ROC curve via grid search. The operating threshold was set to achieve the sensitivity of 90%.

## 2.3 RESULTS

### 2.3.1 Feature Analysis

The processing time for pre-processing, nuclear segmentation, and feature calculation of each image was 0.55 ( $\pm 0.19$ ) seconds. Figure 2.6 shows a set of two-dimensional scatter plots of two related features. As shown in Fig. 2.6a, nuclear intensity was higher, and intensity slope was more negative in HSIL than in non-dysplastic or LSIL. The more negative slope, or more signal attenuation over depth, in HSIL can be explained by the stronger nuclear scattering and higher cell density in HSIL. Nuclear-to-nuclear distance was smaller, and N/C ratio was larger in HSIL (Fig. 2.6b), which is in good agreement with the pathologists' assessment of sLSM images of HSIL: enlarged and crowded nuclei. While cell density was higher in HSIL, nuclear area did not reveal noticeable difference between three categories (y-axis of Fig. 2.6c). Proportion of nuclear pixels, which is essentially the product of cell density and nuclear area, was larger in HSIL than in non-dysplastic or LSIL (Fig. 2.6d).

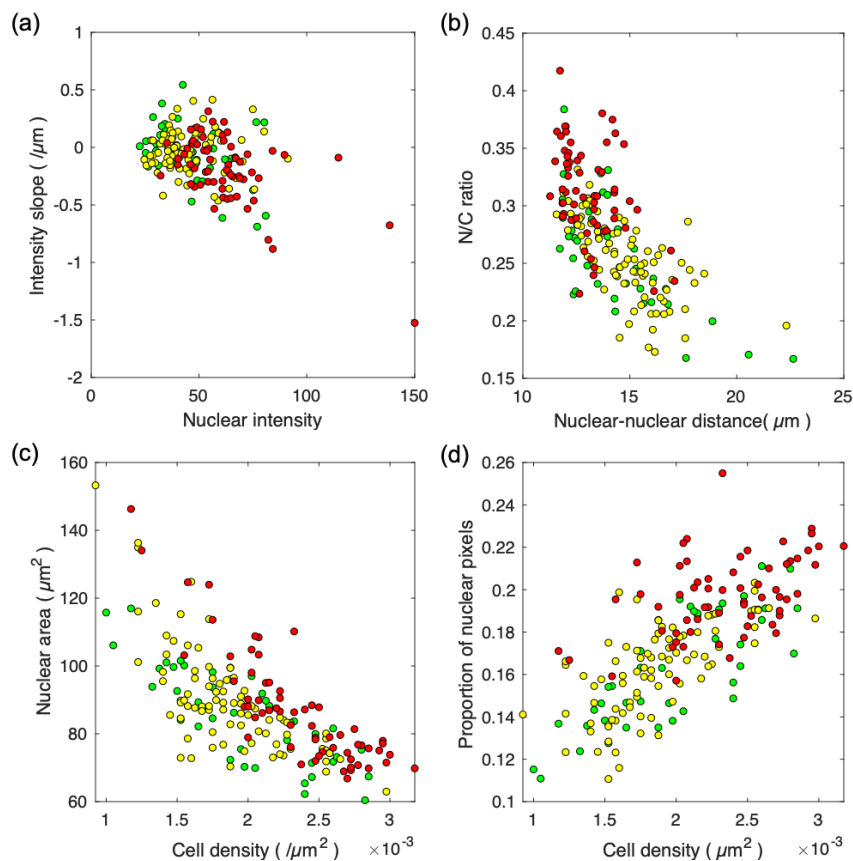


**Figure 2.6:** Two-dimensional scatter plots of feature distributions for three diagnostic categories: non-dysplastic (green), LSIL (yellow), and HSIL (red). (a) Nuclear intensity versus intensity slope, (b) nuclear-to-nuclear distance versus N/C ratio, (c) cell density versus nuclear area, and (d) cell density versus proportion of nuclear pixels.

Figure 2.7 shows a set of scatter plots for each feature along with the average of the feature for each diagnostic category. The trends observed in two-dimensional scatter plots (Fig. 2.6) are also noted in Fig. 2.7: higher intensity, more negative intensity slope, smaller nuclear-to-nuclear distance, larger N/C ratio, higher cell density, and larger proportion of nuclear pixels in HSIL images. Nuclear area did not show statistically significant differences between the three diagnostic categories. Four of the morphologic features were analyzed in the previous confocal microscopy study [11] (nuclear-nuclear distance, N/C ratio, cell density, nuclear area). Three of these features showed similar trends to those found in confocal microscopy images of HSIL: smaller nuclear-to-nuclear distance, larger N/C ratio, and higher cell density than those in non-dysplastic or LSIL images. While the previous confocal microscopy study found that

nuclear area of non-dysplastic was significantly different from that of LSIL or HSIL, the same trend was not observed in sLSM images. The same confocal microscopy study found no significant differences in nuclear area between LSIL and HSIL, which agreed with our finding.

Results from one-way ANOVAs and multiple comparisons are summarized in Table 2.1.

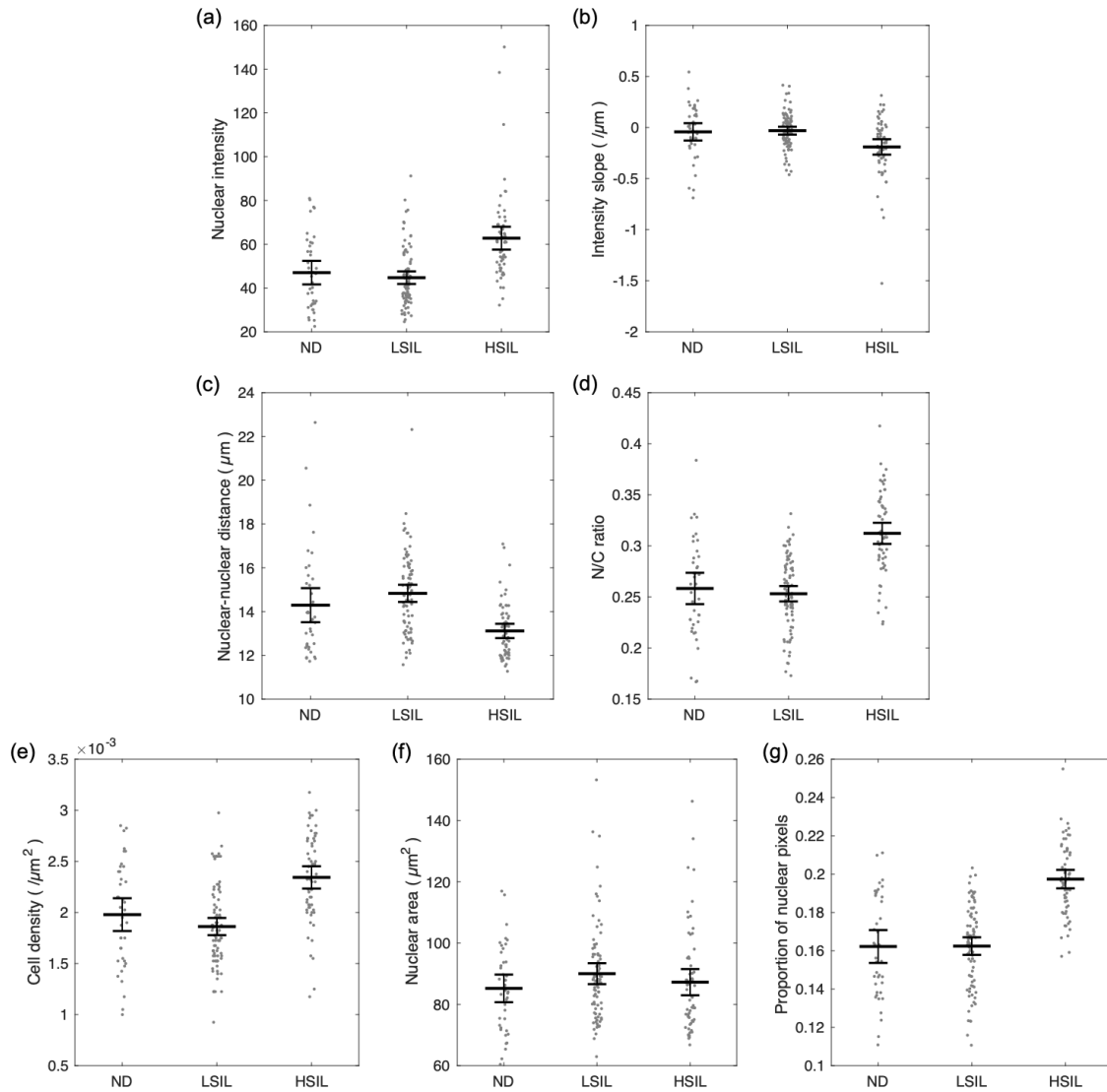


**Figure 2.7:** Scatter plots of features and their average values with 95% confidence intervals. (a) nuclear intensity, (b) intensity slope, (c) nuclear-to-nuclear distance, (d) N/C ratio, (e) cell density, (f) nuclear area, and (g) proportion of nuclear pixels. ND – non-dysplastic.

**Table 2.1:** One-way ANOVAs and multiple comparisons between non-dysplastic (ND), LSIL, and HSIL.

Features	ANOVA p-value	Multiple comparison p-value		
		HSIL vs. ND	HSIL vs. LSIL	ND vs. LSIL
Nuclear intensity	<0.001	<0.001	<0.001	1
Intensity slope	<0.001	0.009	<0.001	1
Nuclear-nuclear distance	<0.001	0.005	<0.001	0.37
N/C ratio	<0.001	<0.001	<0.001	1
Cell density	<0.001	<0.001	<0.001	0.47
Nuclear area	0.25	1	0.89	0.35
Proportion of nuclear pixels	<0.001	<0.001	<0.001	1

### 2.3.2 Classifier Performance

The processing time for generating the classification score from the seven features of each image was short,  $4.0 \times 10^{-5}$  ( $\pm 2.3 \times 10^{-5}$ ) seconds. The ROC curve for per-image diagnosis is shown in Fig. 2.8a. At the operating point providing the sensitivity of 90% (red circle in Fig. 2.8a), the specificity was 70%, and accuracy 77%. The AUC was 0.89. The ROC curve for per-biopsy diagnosis is shown in Fig. 2.8b. At the operating point with the sensitivity of 90%, the specificity was 80%, and accuracy 84%. The AUC for per-biopsy diagnosis was 0.92. The performance of the automated classification was comparable to manual diagnosis of sLSM (blue squares) and H&E images (green squares) as summarized in Table 2.2 [18].

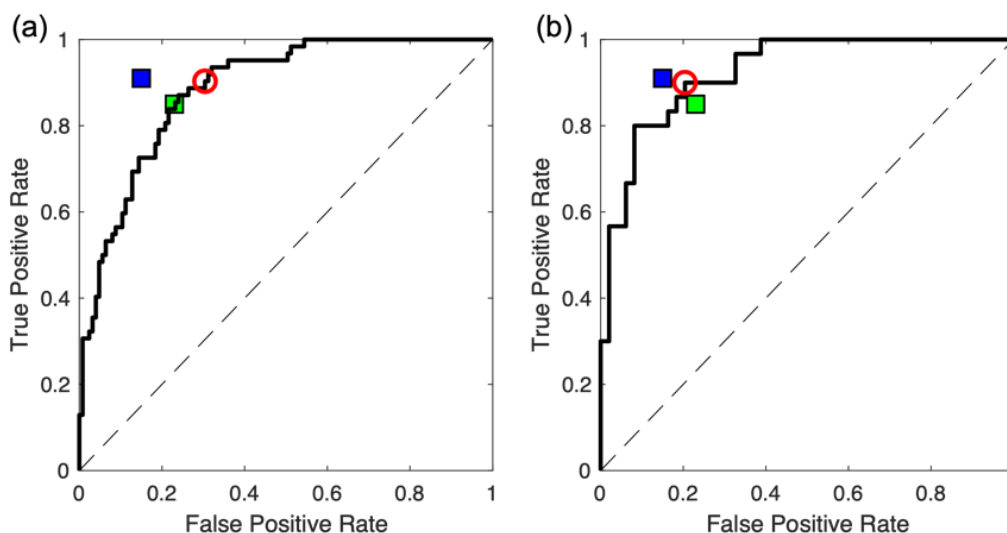


**Figure 2.8:** ROC curves for diagnostic performance evaluation. (a) ROC curve for per-image diagnosis, and (b) ROC curve for per-biopsy diagnosis. red circles – operating points for automated classification, green square – operating point for manual diagnosis of H&E images, and blue square – operating point for manual diagnosis of sLSM images.

**Table 2.2:** Sensitivity, specificity, and accuracy (95% confidence interval) of automated classification of sLSM images in comparison to those of manual diagnosis of sLSM and H&E images.

	<b>Sensitivity</b>	<b>Specificity</b>	<b>Accuracy</b>
Automated sLSM per-image classification	90% (80-95%)	70% (61-77%)	77% (70-82%)
Automated sLSM per-biopsy classification	90% (74-97%)	80% (66-89%)	84% (74-90%)
Manual sLSM diagnosis	91% (81-96%)	85% (77-90%)	87% (81-91%)
Manual H&E diagnosis	85% (73-92%)	77% (68-84%)	80% (73-85%)

Of the 80 biopsies included in sLSM image analysis, 35 were submitted for p16 immunohistochemistry staining per standard of care. p16 staining is used when H&E-stained images are morphologically ambiguous in diagnosing anal intraepithelial neoplasia 2 (AIN2), a type of HSIL, versus LSIL or reactive metaplasia [8]. Among the 35 biopsies submitted for p16 staining, 17 were non-HSIL, and 18 were HSIL per final pathology report. We evaluated the differences of classification scores between biopsies that underwent p16 staining and those that did not. As shown in Fig. 2.9, classification scores for non-HSIL biopsies with p16 staining (black circles) were higher than the scores for those without ( $p\text{-value} = 9.6 \times 10^{-7}$ ). Conversely, HSIL biopsies analyzed with p16 staining (black circles) had lower classification scores

compared to those without ( $p\text{-value} = 1.28 \times 10^{-2}$ ). The overlap in classification scores between non-HSIL and HSIL images was greater for biopsies with p16 staining. The  $d'$  value, calculated by dividing the difference between the means of non-HSIL and HSIL scores by the square root of their average variance, was 1.05 for the p16 group and 2.14 for non-p16 group.

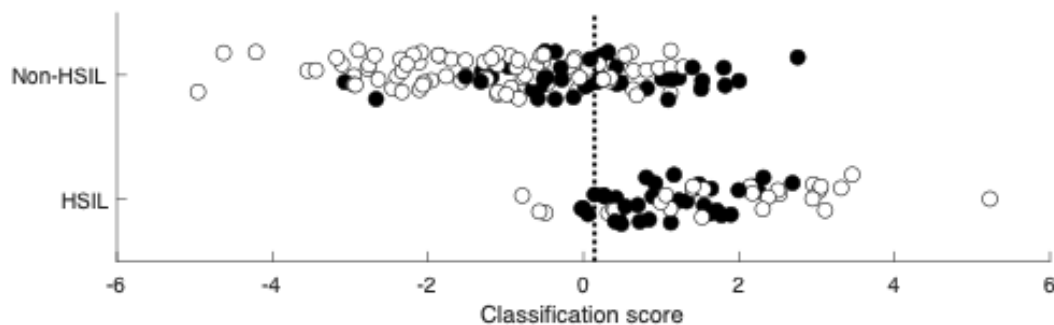


**Figure 2.9:** Classification scores for non-HSIL and HSIL images. black circles – scores for images of biopsies that went through p16, and white circles – scores for images without p16.

## 2.4 DISCUSSION AND CONCLUSION

In this paper, we presented the development of an automated algorithm for analyzing sLSM images of anal squamous intraepithelial lesions. We developed a rule-based, row-by-row binarization method for automatically segmenting sLSM images for nuclei. The segmentation method provided a high precision and recall when compared with manual segmentation. Among the seven features extracted from segmented nuclei, six showed statistically significant difference between HSIL and non-dysplastic or LSIL.

The diagnostic performance of the trained classifier was promising. The linear SVM classifier demonstrated good per-image diagnostic performance (sensitivity = 90%, specificity = 70%) and also good per-biopsy diagnostic performance (sensitivity = 90%, specificity = 80%). The per-biopsy sensitivity and specificity were similar to those of manual analysis of sLSM images by 11 pathologists, 91% and 85%, respectively. Additionally, the per-biopsy diagnostic performance was comparable to that of other optical imaging methods successfully

evaluated for *in vivo* diagnosis of HSIL, including a/LCI (sensitivity = 100%, specificity = 71-82%) and HRME (sensitivity = 91%, specificity = 87%) [9, 14, 15].

In this work, use of the rule-based method of segmenting nuclei and extracting features showed promising diagnostic performance. However, we expect that the rule-based method will face challenges when there is debris above the tissue surface, the surface is fragmented or folded, or the keratinized layer is thick on the surface. Additionally, the rule-based method was slow, 0.55 seconds for calculating seven features per image, and might not have captured some of the key morphologic features pathologists use. Deep learning-based methods could achieve high diagnostic performance for these potentially challenging cases, decrease the processing speed, and improve overall diagnostic performance beyond what is achievable with rule-based methods. In the future, we will explore various deep learning methods of using a convolutional neural network (CNN) followed by a fully-connected network [14, 23] for analyzing sLSM images.

The image analysis algorithm and its diagnostic performance were optimized for the use case of guiding biopsy during high-resolution anoscopy. The biopsy tissues imaged by sLSM were those deemed suspicious per expert anoscopist's assessment of high-resolution anoscopy images. These tissues, especially those determined non-dysplastic per final pathology report, might show different sLSM features than the tissues appearing normal under high-resolution anoscopy. Therefore, for a different use case such as imaging the entire anal canal with a miniaturized sLSM probe as a first-line screening method, a new set of sLSM images will need to be obtained from normal-looking tissue areas and used to refine the image analysis algorithm.

One challenge in using sLSM for guiding anal biopsy can be its small FOV. In this study, 500  $\mu\text{m}$  was used as the FOV, which is similar to the high-power field diameter used during histopathologic analysis of H&E slides. However, the sLSM FOV is significantly smaller than

the diameter of the anal tissue accessible through the anoscope, 15 mm. Our current plan is to have the sLSM probe manually maneuvered by the anoscopist. Therefore, any tissue locations deemed benign or low-grade by the anoscopist will not be imaged by sLSM. This can be problematic because there is a shortage of trained anoscopists and diagnostic performance of high-resolution anoscopy needs improvement [24-26]. A potential solution to address this issue is systematic sLSM imaging of pre-determined tissue locations (e.g. at every quadrant of the circular tissue area accessible for imaging at the distal end of the anoscope) in addition to the tissue locations deemed high-grade per anoscopist's assessment. Another direction is using deep learning-based methods to analyze high-resolution anoscopy images and identify high-risk tissue areas [27] and image the deep learning-identified tissue areas with sLSM . This approach can be helpful in guiding anoscopists, especially those with less experience in high-resolution anoscopy.

## **FUNDING**

National Institutes of Health (R21EB030079, P30CA023074).

## **ACKNOWLEDGMENTS**

We thank the patients from the Stanford PEACH (Prevention and Education of Anogenital Cancers and HPV-associated diseases) program who took part in this study. We would like to thank Stanford Health Care medical assistant Jonathan Contreras-Quevedo who helped with the logistics of obtaining and imaging biopsy samples for this study. We would like to thank Amie Wong, NP of the Stanford PEACH Program who helped with obtaining the samples for imaging.

## **DISCLOSURES**

The University of Arizona has a technology-licensing agreement with ArgosMD on the

reflectance confocal microscopy technology. DK has the rights to receive royalties as a result of this licensing agreement. DK serves as a scientific advisor to ArgosMD. Conflicts of interest resulting from this interest are being managed by the University of Arizona in accordance with its policies.

#### **DATA AVAILABILITY**

The data that support the findings of this study are available from the corresponding author upon reasonable request.

### CHAPTER 3

### CONCLUSIONS

sLSM has shown its capability to visualize nuclear morphological features critical for identifying dysplastic changes in tissue. Our study validated the potential of sLSM as an automated diagnostic tool for anal squamous intraepithelial lesions through the implementation of row-by-row binarization method for segmenting nuclei in sLSM images. This approach effectively addressed challenges associated with depth-dependent intensity variation.

The automated algorithm using these features demonstrated reliable diagnostic performance comparable to manual histopathological evaluations. Additionally, The results showed that our algorithm could distinguish HSIL from non-HSIL with sensitivity and specificity similar to other advanced imaging methods. These findings indicate that sLSM has potential as a supplemental diagnostic tool to improve biopsy precision and facilitate the early detection of precancerous lesions.

While the results are promising, certain limitations still need to be addressed. The current approach relies on rule-based methods for feature extraction, which may struggle with complex tissue variations. Addressing these challenges is critical to improving the diagnostic performance. In the future, we will focus on enhancing the classification method through the deep learning algorithms, such as convolutional neural networks. These methods could identify subtle morphological features that are not evident with rule-based methods. Furthermore, the development of a miniaturized sLSM probe is essential to enable *in vivo* imaging in clinical settings. The final goal is integration of miniaturized sLSM probe with real-time deep learning-based diagnosis to further enhance the utility of sLSM as a non-invasive diagnostic tool.

## REFERENCES

1. H. Siedentopf and R. Zsigmondy, "Visualization and size measurement of ultramicroscopic particles, with special application to gold-colored ruby glass," *Ann. Phys* **10**, 1-39 (1903).
2. J. Huisken, J. Swoger, F. Del Bene, et al., "Optical sectioning deep inside live embryos by selective plane illumination microscopy," *Science* **305**, 1007-1009 (2004).
3. A. A. Deshmukh, R. Suk, M. S. Shiels, et al., "Recent trends in squamous cell carcinoma of the anus incidence and mortality in the United States, 2001–2015," *JNCI: Journal of the National Cancer Institute* **112**, 829-838 (2020).
4. N. C. I. Surveillance Research Program, "SEER\* Explorer: an interactive website for SEER cancer statistics," (National Cancer Institute Bethesda, MD, 2023).
5. J. M. Palefsky, J. Y. Lee, N. Jay, et al., "Treatment of anal high-grade squamous intraepithelial lesions to prevent anal cancer," *New England journal of medicine* **386**, 2273-2282 (2022).
6. M. A. Clarke, A. A. Deshmukh, R. Suk, et al., "A systematic review and meta-analysis of cytology and HPV-related biomarkers for anal cancer screening among different risk groups," *International journal of cancer* **151**, 1889-1901 (2022).
7. J. R. Mourant, T. M. Powers, T. J. Bocklage, et al., "In vivo light scattering for the detection of cancerous and precancerous lesions of the cervix," *Applied optics* **48**, D26-D35 (2009).

8. T. M. Darragh, T. J. Colgan, J. T. Cox, et al., "The lower anogenital squamous terminology standardization project for HPV-associated lesions: background and consensus recommendations from the College of American Pathologists and the American Society for Colposcopy and Cervical Pathology," *Archives of pathology & laboratory medicine* **136**, 1266-1297 (2012).
9. D. Ho, T. K. Drake, K. K. Smith-McCune, et al., "Feasibility of clinical detection of cervical dysplasia using angle-resolved low coherence interferometry measurements of depth-resolved nuclear morphology," *International journal of cancer* **140**, 1447-1456 (2017).
10. T. Collier, M. Guillaud, M. Follen, et al., "Real-time reflectance confocal microscopy: comparison of two-dimensional images and three-dimensional image stacks for detection of cervical precancer," *Journal of Biomedical Optics* **12**, 024021-024021-024027 (2007).
11. F. Sheikhzadeh, R. K. Ward, A. Carraro, et al., "Quantification of confocal fluorescence microscopy for the detection of cervical intraepithelial neoplasia," *Biomedical engineering online* **14**, 96 (2015).
12. B. Hunt, J. H. T. G. Fregnani, R. A. Schwarz, et al., "Diagnosing Cervical Neoplasia in Rural Brazil Using a Mobile Van Equipped with In Vivo Microscopy: A Cluster-Randomized Community Trial," *Diagnosing Cervical Neoplasia in Rural Brazil," Cancer Prevention Research* **11**, 359-370 (2018).
13. S. G. Parra, L. M. López-Orellana, A. R. Molina Duque, et al., "Cervical cancer prevention in El Salvador: a prospective evaluation of screening and triage strategies incorporating high-resolution microendoscopy to detect cervical precancer," *International journal of cancer* **148**, 2571-2578 (2021).

14. D. Brenes, C. Barberan, B. Hunt, et al., "Multi-task network for automated analysis of high-resolution endomicroscopy images to detect cervical precancer and cancer," *Computerized Medical Imaging and Graphics* **97**, 102052 (2022).
15. D. Brenes, A. Kortum, J. Coole, et al., "Deployment and assessment of a deep learning model for real-time detection of anal precancer with high frame rate high-resolution microendoscopy," *Scientific reports* **13**, 22267 (2023).
16. J. Zhao, N. Kulkarni, E. Dobo, et al., "Investigation of different wavelengths for scattering-based light sheet microscopy," *Biomedical Optics Express* **13**, 3882-3892 (2022).
17. C. D. Nguyen, P. K. O'Neal, N. Kulkarni, et al., "Scattering-based light-sheet microscopy for rapid cellular imaging of fresh tissue," *Lasers in surgery and medicine* **53**, 872-879 (2021).
18. B. Liang, J. Zhao, Y. Kim, et al., "Scattering-Based Light-Sheet Microscopy Imaging of Human Papillomavirus–Associated Squamous Lesions of the Anal Canal: A Proof-of-Principle Study," *Modern Pathology* **37**, 100493 (2024).
19. J. Zhao, Y. Kim, M. Sugimura, et al., "Compact scattering-based light sheet microscopy probe using a custom miniature objective lens," *Journal of Optical Microsystems* **4**, 034501-034501 (2024).
20. N. Otsu, "A threshold selection method from gray-level histograms," *Automatica* **11**, 23-27 (1975).
21. S. R. Sternberg, "Biomedical image processing," *Computer* **16**, 22-34 (1983).
22. U. Schmidt, M. Weigert, C. Broaddus, et al., "Cell detection with star-convex polygons," in *Medical Image Computing and Computer Assisted Intervention–*

*MICCAI 2018: 21st International Conference, Granada, Spain, September 16-20, 2018, Proceedings, Part II 11*, (Springer, 2018), 265-273.

23. M. Saini and S. Susan, "Vggin-net: Deep transfer network for imbalanced breast cancer dataset," *IEEE/ACM Transactions on Computational Biology and Bioinformatics* **20**, 752-762 (2022).
24. O. Richel, N. D. Hallensleben, A. Kreuter, et al., "High-resolution anoscopy: clinical features of anal intraepithelial neoplasia in HIV-positive men," *Diseases of the colon & rectum* **56**, 1237-1242 (2013).
25. W. C. Mathews, A. Sitapati, J. C. Caperna, et al., "Measurement characteristics of anal cytology, histopathology, and high-resolution anoscopic visual impression in an anal dysplasia screening program," *JAIDS Journal of Acquired Immune Deficiency Syndromes* **37**, 1610-1615 (2004).
26. C. Mathews, J. Caperna, E. R. Cachay, et al., "Early impact and performance characteristics of an established anal dysplasia screening program: program evaluation considerations," *The open AIDS journal* **1**, 11 (2007).
27. M. Saraiva, L. Spindler, N. Fathallah, et al., "Artificial intelligence and high-resolution anoscopy: automatic identification of anal squamous cell carcinoma precursors using a convolutional neural network," *Techniques in Coloproctology* **26**, 893-900 (2022).